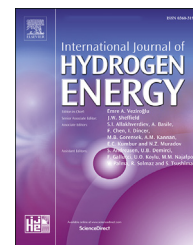Available online at www.sciencedirect.com

ScienceDirect

journal homepage: www.elsevier.com/locate/he

X-ray tomography and modelling study on the mechanical behaviour and performance of metal foam flow-fields for polymer electrolyte fuel cells

A. Fly [a], Q. Meyer [b,c], M. Whiteley [b], F. Iacoviello [b], T. Neville [b],
P.R. Shearing [b], D.J.L. Brett [b], C. Kim [d], R. Chen [a,*]

[a] Department of Aeronautical and Automotive Engineering, Loughborough University, Loughborough, LE11 3TU, United Kingdom
[b] Electrochemical Innovation Lab, Department of Chemical Engineering, University College London, London, WC1E 7JE, United Kingdom
[c] Nanoelectrochemistry Group, School of Chemistry, UNSW, Sydney 2052, Australia
[d] Korea Institute of Energy Research, Daejeon, South Korea

ARTICLE INFO

ABSTRACT

Porous metal foams have been used as alternative flow-fields in proton exchange membrane fuel cells (PEMFCs), exhibiting improved performance compared to conventional 'land and channel' designs. In the current work, the mechanical behaviour of PEMFCs using metal foam flow-fields is investigated across different length scales using a combination of electrochemical testing, X-ray computed tomography (CT), compression tests, and finite element analysis (FEA) numerical modelling.

Fuel cell peak power was seen to improve by 42% when foam compression was increased from 20% to 70% due to a reduction in the interfacial contact resistance between the foam and GDL. X-ray CT scans at varying compression levels reveal high levels of interaction between the metal foam and gas diffusion layer (GDL), with foam ligaments penetrating over 50% of the GDL thickness under 25% cell compression. The interfacial contact area between the foam and GDL were seen to be 10 times higher than between the foam and a stainless-steel plate. Modelling results demonstrate highly uniform contact pressure distribution across the cell due to plastic deformation of the foam. The effect of stack over-tightening and operating conditions are investigated, demonstrating only small changes in load distribution when paired with a suitable sealing gasket material.

© 2019 The Author(s). Published by Elsevier Ltd on behalf of Hydrogen Energy Publications LLC. This is an open access article under the CC BY license (http://creativecommons.org/licenses/by/4.0/).

Introduction

The management of reactant gas distribution and product water removal in proton exchange membrane fuel cells (PEMFCs) is essential in maximising fuel cell performance and preventing flooding due to excess accumulation of liquid water [1]. The most widely utilised method of reactant distribution in PEMFCs is through flow channels that are machined, pressed or etched into the bipolar plate (BPP) [2]. The 'channel' area is used for gas distribution and product water removal, whereas the remaining 'land' area is in contact with the gas diffusion layer (GDL) to facilitate electron transport, waste heat removal and structural integrity [3]. The arrangement of the land and channel geometry for improving fuel cell performance has seen extensive study in the literature. Wang et al. [4] studied the optimum land-to-channel geometry of a PEMFC flow-field, concluding that an equal land and channel area of 0.5 mm width and 0.5 mm depth gave optimum performance. Many studies have been conducted to evaluate the different arrangements of flow channels for even reactant distribution across the surface of the cell [5]. Sasmito et al. [6] conducted numerical studies comparing six different flow-field designs, evaluating current density and temperature distribution as well as parasitic pumping losses. Whereas Liu et al. [7] experimentally studied seven different flow-field patterns for optimum flow distribution, with the serpentine flow channel showing the best performance. Of the many different flow channel designs studied in the literature, the most commonly used is the multi-serpentine design due to its reduced pressure drop compared to a single serpentine design, but improved water removal compared to a parallel channel design [3].

Whilst the land and channel design has seen extensive use, there are some inherent disadvantages of this design. At high current densities, product water can accumulate under the land area, restricting diffusion of reactant gas across the GDL and lowering performance [4]. This phenomenon was experimentally observed by Meyer et al. [8,9] using neutron radiography. Contact between the BPP and GDL is also uneven, with high contact pressures under the land area and no contact pressure in the channel areas; this can lead to uneven compression of the GDL, as observed by Mason et al. [10]. Kusoglu et al. [11] also demonstrated high levels of membrane shear stress at the transition between the land and the channel during hydration using a finite element analysis (FEA) model.

Several alternatives to conventional flow-fields have been proposed in the literature, including porous flow-fields [12], interdigitated flow-fields [5] and three-dimensional lung-inspired flow-fields [13]. Flow-fields utilising open cell porous metallic foam flow-fields have seen increased interest due to high porosity (>85%), high thermal conductivity and low electrical resistance [12,14—18]. Metallic foam flow-fields were first used as PEMFC flow-fields by Murphy et al. [19] who tested an eight-cell 520 W fuel cell stack using gold plated nickel foam. Kumar and Reddy [20,21] compared the performance of stainless steel foam, Ni—Cr foam and conventional multi-serpentine machined flow channels; demonstrating improved performance of the Ni—Cr foam compared to the conventional flow-fields, especially in the mass transport region. Modelling studies by the same authors [22] showed

increased performance was due to a reduction in flow channel permeability, at the expense of increased pressure drop. More recently, numerous studies have been conducted using metallic foam flow-fields in PEMFCs. Including the influence of foam cell size [23], cold start behaviour [24], water transport [25,26], flow-field separators [27], flow distribution [28,29] and graphene coatings for increased corrosion resistance [30,31].

X-ray CT scanning and reconstruction techniques are highly insightful ways in which to non-destructively analyse fuel cell materials. X-ray CT has been used to great effect in the fuel cell field of research, such as the analysis of GDL materials [32—34]. A recent study by Jinuntuya et al. [35] used X-ray CT techniques to scan three different constructions of GDLs. The scans were then reconstructed to form a 3D model of the material to be then used in a Lattice-Boltzmann simulation of water flow through the material. More recently, Hack et al. [36] used X-ray CT techniques to analyse the mechanical structure and durability differences between different methods of a fuel cell assembly. The behaviour of the carbon fibres under compression has been of particular interest [37—42] to recreate and understand the deformations occurring to the fibres under a flow field, revealing a reduction in porosity and tortuosity that is directly affected by the type of GDL and initial porosity.

These techniques allow analysis of the structure of fuel cells, and the scans can then be reconstructed to form a model of the materials. Further modelling research can then be undertaken *in silico* such as porosity-tortuosity analysis, flow modelling, and even mechanical analysis.

Whilst there have been numerous studies investigating the performance of metallic foam fuel cells, the influence on mechanical behaviour has not been studied. In this paper, the mechanical behaviour of metallic foam flow-fields has been studied from the micro-scale interactions between the foam and GDL, to macro-scale behaviour at cell and stack level. A combination of experimental analysis, X-ray computed tomography and finite element modelling is used, with comparisons drawn to conventional land and channel designs.

Experimental

The following sections detail the experimental tests conducted to characterise the mechanical behaviour of metallic foam flow-fields in PEMFCs. All tests were conducted using 1.6 mm thick commercial nickel foam sheets (Corun New Energy, China). Table 1 shows details of the foam properties; parameters are either taken from the manufacturer's specification or obtained from the X-ray CT scans detailed in Section Electrochemical testing.

Table 1 — Open-cell nickel foam parameters.

Parameter	Value	Source
Thickness	1.6 mm	Manufacturer
Cell size	110 ppi	Manufacturer
Density	262.5 kg m^{-3}	Manufacturer
Overall porosity	86.5%	X-ray CT
Flow porosity	84.0%	X-ray CT

Electrochemical testing

The membrane electrolyte assembly (MEA) was constructed by hot pressing a dry Nafion® NRE-212 (Dupont, USA) membrane between two catalyst coated gas diffusion electrodes (GDEs) (ELE0162, Johnson Matthey, UK) at 2760 kPa, 130 °C for 3 min [43]. The GDE consisted of a carbon paper GDL, microporous layer and catalyst layer with 0.4 mg Pt cm^{-2}.

Polarisation and electrochemical impedance spectroscopy (EIS) tests were conducted on a PEMFC with metal foam flow fields at three different compression levels. A 25 cm^2 MEA was placed between foam flow fields which were gold coated for corrosion resistance, gaskets of different thickness (1.5, 1.0 and 0.5 mm) were then used to control the foam compression.

Each cell was conditioned through rapid polarisation curve cycling for ten repetitions, or until the overall cell performance no longer improved. The potential was stepped in 0.05 V increments at 5 s per step. Once the cells were conditioned, a slow polarisation curve was taken and is presented in this work. The voltage was swept at 0.01 V increments at 30 s per point to allow sufficient time to settle at each potential point. All testing was undertaken on an 850e fuel cell test system (Scribner and Associates, USA) using a stoichiometric flow for both anode and cathode gasses of 1.5 and 3 respectively. The cell temperature was 70 °C with gas relative humidity set at 75%. EIS was undertaken using a potentiostat (Gamry Reference 3000, Gamry Instruments USA) with an AC current set at 10% of the cells DC current. Compression of the metal foam flow-field was measured using a digital micrometer when disassembling the cell, this technique is valid for metal foams since elastic deformation under compression is negligible.

X-ray CT

X-ray CT images were collected using a laboratory-based Zeiss XRADIA 520 VERSA (Carl Zeiss X-Ray Microscopy Inc., California) fitted with a CT5000 in-situ compression/tension testing stage (Deben, UK). Two tests were conducted; compression of a single sheet of metal foam and compression of an MEA sandwiched between two metal foam flow-fields.

Two custom made aluminium plates were machined, on which the sample is installed. An X-ray transparent Kapton tube (2.05 mm diameter) was fitted around the aluminium cylinders to enable alignment of the two cylinders and of the samples during assembly and ensure that only vertical displacement of the cylinders occurs during compression (Fig. 1b). In the single sheet compression, a 2.0 mm diameter foam disc was inserted in the assembly (Fig. 1c) and compressed from 1.6 mm thickness to 0.22 mm.

Six scans were conducted during the compression process. At each compression level, 2201 projections were captured using a 5.0 s exposure time and 80 kV source voltage. Image resolution was 5.1 µm per pixel. A camera binning of 4 was used, with an optical magnification of 4 times.

In the foam/MEA compression test a 1.0 mm diameter section of MEA was prepared as described in 2.1 and placed between two sheets of metal foam, representing the structure of a PEMFC with metal foam flow-fields (Fig. 1d).

The MEA and metal foam had not been used in a fuel cell prior to testing. Scans were conducted at 0%, 15% and 25% compression. Each scan contained 1601 projections using a 32 s exposure time and 80 kV source voltage. Image resolution was 1.7 µm per pixel. A camera binning of 4 was used, with an optical magnification of 20 times. A high binning was used due to the difference in density between the foam (high density) and the carbon fibres (low density), to reduce the exposure time while improving image quality, at the detriment of the resolution of the GDL fibres.

Reconstruction of the radiographs into a 3D volume was achieved using a cone-beam filtered back-projection algorithm (Reconstructor Scout-and-Scan, ZEISS). To calculate the interface properties for each component material in the MEA, the normalised interface contact area and material fraction per slice were defined.

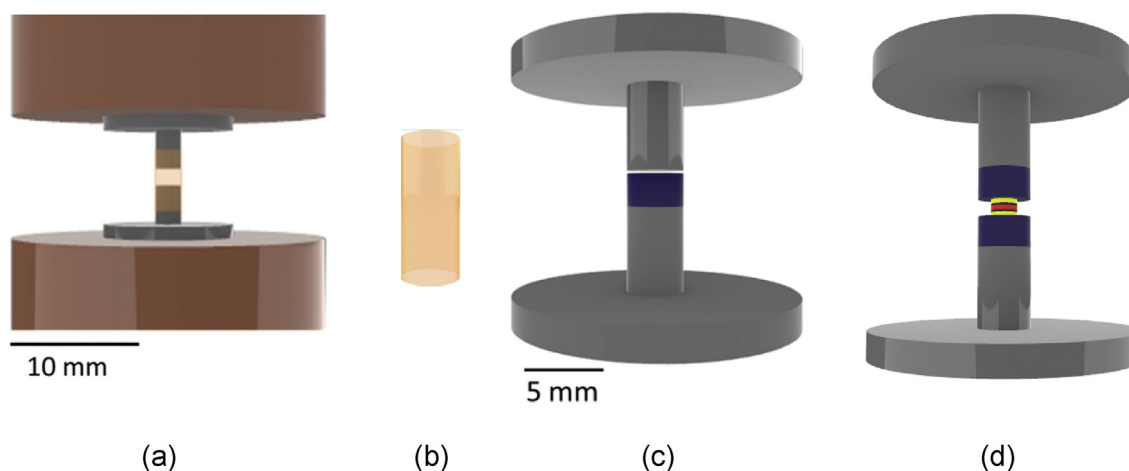The normalised contact area ($A_{i,j}$) between each material in the MEA was calculating using Eq. (1):

10 mm

5 mm

(a)   (b)   (c)   (d)

Fig. 1 − (a) Empty assembly inserted inside the Deben compression stage between the two compression plates (brown), with aluminium cylinders (grey) and Kapton tube (orange). (b) Close up of the Kapton tube, (c) assembly with the 2 mm metal foam (blue) (Kapton tube removed), (d) assembly with the two metal foams and the 1 mm MEA with the GDLs (yellow), MPLC (black) and Nafion membrane (red) (Kapton tube removed). (For interpretation of the references to colour in this figure legend, the reader is referred to the Web version of this article.)

$$A_{i,j} = \frac{a_{i,j}}{A_g} \qquad\qquad 1$$

Where $a_{i,j}$ represents the contact area between materials i and j respectively, determined by the surface area patch modules in Avizo and A_g the geometric surface area.

Then the material fraction per slice ($X_i(z)$) was calculated using Eq. (2):

$$X_i(z) = \frac{n_i(z)}{n} \qquad\qquad 2$$

Where $n_i(z)$ is the number of pixels that are segmented for material i at slice z, and the total number of pixels in the slice n, calculated using ImageJ software. The coexistence of the materials in a slice is considered to be true when two or more materials are visible on subsequent slices through the z axis.

Foam compression tests

Uniaxial compression tests were conducted on the metal foam to ASTM C365 [44] using an 8872 25 kN fatigue testing system (Instron, USA). Tests were conducted on 25 mm diameter circular samples, compressed from 1.60 mm to 0.46 mm at a rate of 0.3 mm per minute, reaching a maximum load of 4.0 kN. Force and displacement were recorded at 2.0 Hz. Six repeats were conducted then averaged; deviation from the mean was less than 10%.

Interfacial contact resistances (ICR)

Resistance measurements were conducted at different compression pressures to isolate the interfacial contact resistances (ICRs) between the GDL, metal foam and the current collector plate. To obtain the measurements, a 5 cm^2 metal foam section was placed between two gold-coated copper plates of the same dimensions, and compressive pressure applied using a controlled compression rig that was manufactured in-house. Resistance was measured using a potentiostat (Gamry Reference 3000, Gamry Instruments USA) with a resolution of $\pm 1\%$. Measurements were taken for the two plates without the foam, with a single foam section between the plates and with a single foam/GDL assembly.

ICR was calculated using the method of El-Kharouf et al. [45]. The measured resistance between the two plates under compression was subtracted from the measured resistance of the same set up with the foam present. The resulting resistance was then divided by two to account for the two interfaces, one with each plate. The difference in resistance with and without the GDL present was used to evaluate the ICR between the foam and GDL. This method assumes that the contact resistance between the two gold-coated plates and through-plane resistance of the foam are both negligible, which is reasonable given the high conductivities of gold and nickel relative to the ICR.

Finite element model

To analyse the mechanical behaviour of the metallic foam at a cell and stack level, a finite element model of a 100 cm^2 active area cell was created in the commercial package Abaqus. The model consists of 20 mm thick steel endplates with eight steel bolts, stainless steel bipolar plates and current collectors, silicone gasket, metal foam flow-field, GDL and membrane. By applying symmetry in the x, y and z planes, only 1/8th of the geometry is modelled, significantly reducing computational resources.

The endplate, BPP, membrane and clamping bolts were all modelled as being linear elastic. Non-linear compressive properties of the gasket and GDL were accounted for using the hyperelastic material model based on uniaxial compression data from Ref. [46]. The metal foam was modelled as a homogeneous volume using the crushable foam hardening material model and experimental data from the current work. Considering the foam as a homogeneous structure does not account for individual foam pore behaviour, but significantly reduces the meshing complexity, allowing cell-level simulations to be conducted. The validity of this assumption is demonstrated by comparing the results of the X-ray CT scans to the 3D FEA in Section Analysis.

A 1.0 mm thick gasket was used in the model to control foam compression and provide a gas-tight seal around the MEA. During assembly, the metal foam flow-field was first compressed before the current collector or bipolar plate contacts the gasket, as illustrated in Fig. 2b. In the FEA model, tangential contact between all components was modelled using a constant 0.3 coefficient of friction and normal contact using the exponential pressure-overclosure model. A compressive load of 1500 N per bolt was applied during initial compression, after which the bolt lengths were fixed, and assembly conditions applied to all components.

The components were meshed using C3D8R elements. Mesh seeds varied between components, ranging between 2.0 mm for the endplate to 0.5 mm for the membrane and GDL. A mesh optimisation study showed that further decreasing mesh seeds resulted in output results variation of less than 1%. The 1/8th model of the five-cell stack contained 70,720 elements.

As identified by Kusoglu et al. [11], the influence of temperature and hydration during operation can have a significant effect on the stress experienced by the membrane. Experiments conducted on Nafion® 112 membranes by Tang et al. [47] showed a 77% reduction in Young's Modulus and 10% volume swelling when moving between 25 °C 30% RH and 85 °C 90% RH. To account for membrane swelling, an equivalent coefficient of expansion (α') [48] was used to represent both thermal expansion of the membrane and swelling due to water uptake as a single value compatible with commercial FEA software. Shown in Eq. (3), where α is the thermal expansion coefficient, ΔT the temperature difference, β the membrane expansion coefficient and $\Delta \lambda$ the change in membrane water content. Variation in membrane stiffness under operational conditions is accounted for using a two-dimensional (temperature and humidity) look-up table for the Young's Modulus from Ref. [48].

$$\alpha' = \frac{\alpha \Delta T + \beta \Delta \lambda}{\Delta T} \qquad\qquad 3$$

A list of the material properties used in the FEA model is shown in Table 5. The model was validated by replicating the compression tests of Section X-ray CT and comparing relative displacement of the MEA components under the same
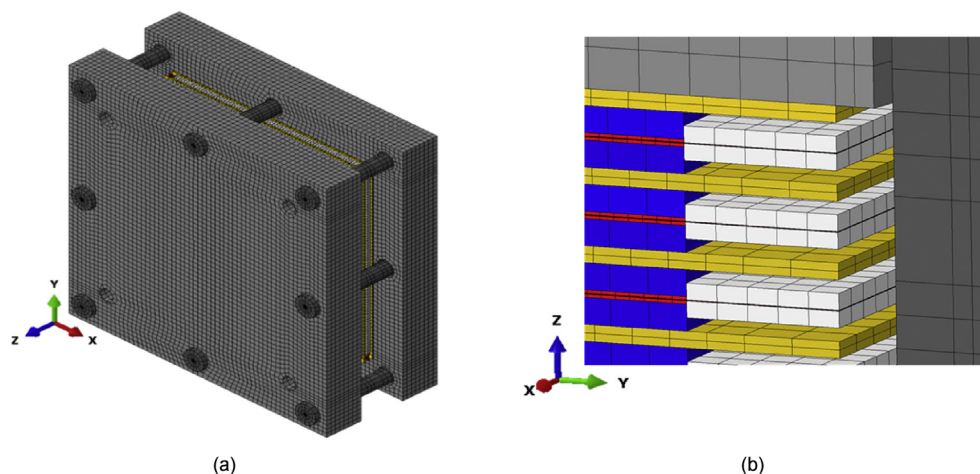
(a)   (b)

Fig. 2 − Uncompressed five cell FEA model of (a) 8 bolt stack and (b) close up cross section of foam/gasket spacing. Blue - metal foam, white - gasket, red - MEA, gold - BPP, light/dark grey - endplate/bolts. (For interpretation of the references to colour in this figure legend, the reader is referred to the Web version of this article.)

compression conditions as the X-ray CT results. Validation results are discussed in Section Analysis. In addition to the metal foam flow-field, a conventional multi-serpentine channel in a graphite bipolar plate was also modelled for comparison.

Analysis

Effect of foam compression on electrochemical performance

The polarisation curves and EIS of the foam flow-fields in a working cell at different overall foam compressions are shown in Fig. 3. Increasing compression is seen to improve performance within the region tested, primarily due to a reduction in contact resistance of the cell as demonstrated by the reduction in high frequency intercept in Fig. 3b. Higher levels of foam flow-field compression also increase mass transport losses due to a reduction in flow field porosity influencing reactant distribution

and product water removal. Increasing mass transport losses can be seen in the establishment of a low frequency arc at the highest compression in Fig. 3b. For all the flow rates and compression levels tested, pressure drop across the foam flow-field did not exceed 100 mBar, the three increasing compression levels correspond the foam porosities of 86.8, 83.2 and 72.7% respectively based on interpolation of Table 2.

The ICR measurements of the foam with and without a GDL are shown in Fig. 4 and allow the foam contact resistances to be studied independently of the MEA. The contact resistances between the foam and plate, and between the foam and GDL, are comparable to the lowest interfacial resistances between a conventional GDL and graphite plate [45]. The low interfacial resistance between the metal foam and GDL is due to the intrusion of foam ligaments into the GDL, increasing the normalised contact area. To enhance the understanding of this process, the compression of the cell with metal foams is studied in extensive details.
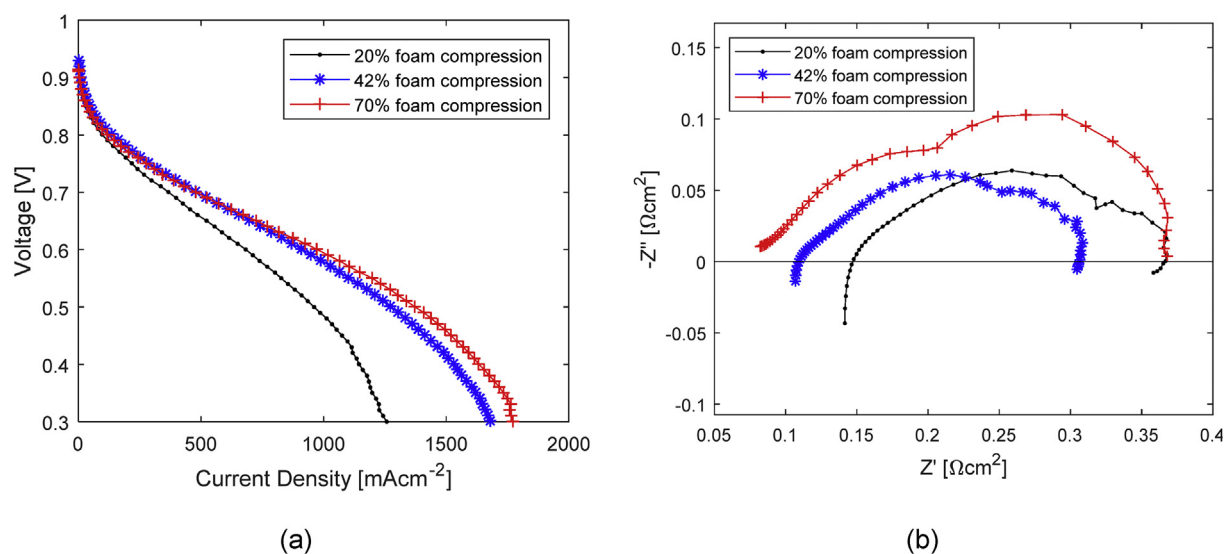

(a)   (b)

Fig. 3 − Influence of foam flow-field compression on fuel cell performance (a) Polarisation curves, (b) EIS at 800 mAcm^{-2}.

Table 2 – Results from foam compression experiments.

Thickness (mm)	Compression level (%)	Normalised interfacial contact (%)	Porosity (%)	Average pore volume (mm^3)	Stress (MPa)
1.45	0.00	0.10	89.15	0.018641	0.19
1.20	17.27	3.14	87.46	0.018445	0.64
0.95	34.53	6.52	83.46	0.014856	0.89
0.70	51.80	7.86	82.77	0.010420	1.35
0.45	69.06	11.20	73.66	0.006194	2.46
0.20	86.33	17.14	55.39	0.001510	—

Foam compression

The deformation of the foam structure is clearly visible at the different compression levels (Fig. 5). The porosity of the sample under compression was calculated from the X-ray CT data, as described in Section X-ray CT, the volumes above and below the foam sample at 0% compression were removed from the porosity analysis. Foam porosity (ϕ) is reduced under compression as the gas volume (V_{gas}) reduces as a fraction of the total volume (V_{total}), Eq. (4). The theoretical change in porosity (ϕ_{theo}) with compression (x) can be determined from the zero-compression porosity (ϕ_0) using Eq. (5), assuming only the gas volume is reduced during compression.

$$\phi = \frac{V_{gas}}{V_{total}} \qquad 4$$

$$\phi_{theo} = \frac{\phi_0 - x}{1 - x} \qquad 5$$

The theoretical and measured foam porosities under compression are compared in Fig. 6a. Good agreement is seen at compression levels below 50%; however, as compression increases the theoretical porosity under-predicts the measured porosity, implying that the volume inaccessible to fluid flow is also reducing at higher loads. This occurs due to the compression of voids in the foam ligaments created during the manufacturing process. These voids are not included in the calculation of V_{gas} since they are inaccessible to fluid flow; however, their volume is included in V_{total}. It is therefore

important to consider these effects if compression levels greater than 50% are to be used.

The foam properties measured under compression are shown in Table 2, normalised interfacial contact area is seen to increase linearly with compression and average pore volume decrease linearly after the initial elastic compression region. The increased contact area between the foam and platens leads to reduced interfacial resistances, whereas decreasing average pore volume increases the pressure drop through the foam. The optimum compression for a PEMFC must therefore compromise between minimising both ICR and parasitic loads for maximum performance.

The relationship between compressive load and material thickness is shown in the stress-strain curve of Fig. 6b. As with other metallic foam structures, the stress-strain relationship shows three distinct regions with different gradients: the elastic region (up to 0.08 strain), the plateau region (0.08—0.55 strain) and the densification region (above 0.55 strain) [49]. In the plateau region, individual ligaments within the foam are being plastically deformed, reducing the gas volume and hence porosity. The load increment required to deform each ligament is small compared to the total load applied, resulting in a lower gradient (stiffness) in this region. As the strain is increased, the material enters the densification region in which the deformed ligaments contact each other and the material stiffness approaches that of the solid bulk material. The transition between the plateau and densification regions is also seen to coincide with the point at which the theoretical and measured porosities diverge in Fig. 6a.

Under conventional fuel cell compression pressures (1.0—1.5 MPa [50]) the foam transitions between the plateau and densification regions. The large amount of plastic deformation during assembly is beneficial in providing even load distribution across the surface of the MEA and absorbing small deflections in the endplate. However, over-compression of the fuel cell stack will lead to irreversible compression of the flow-fields. For a flow-field depth of 0.8 mm, the measured porosity of the foam would be 83.1%, the normalised interfacial contact area 7.32% and 1.14 MPa of compression required.

The stress-strain relationship of the FEA model is compared to the experimental results in Fig. 6a, showing an excellent fit with only minimal deviations in the elastic region due to the linear assumption of the model.

MEA compression

Three-dimensional reconstructions from the X-ray CT scans of the foam flow-field and MEA under compression are shown in Fig. 7a, b and e. To achieve a suitable resolution at the GDL length
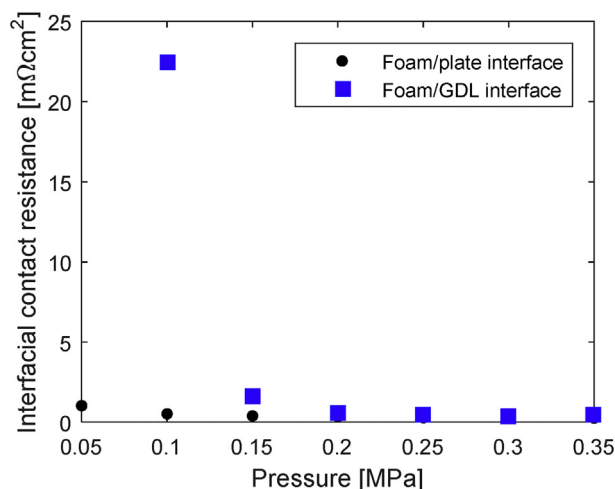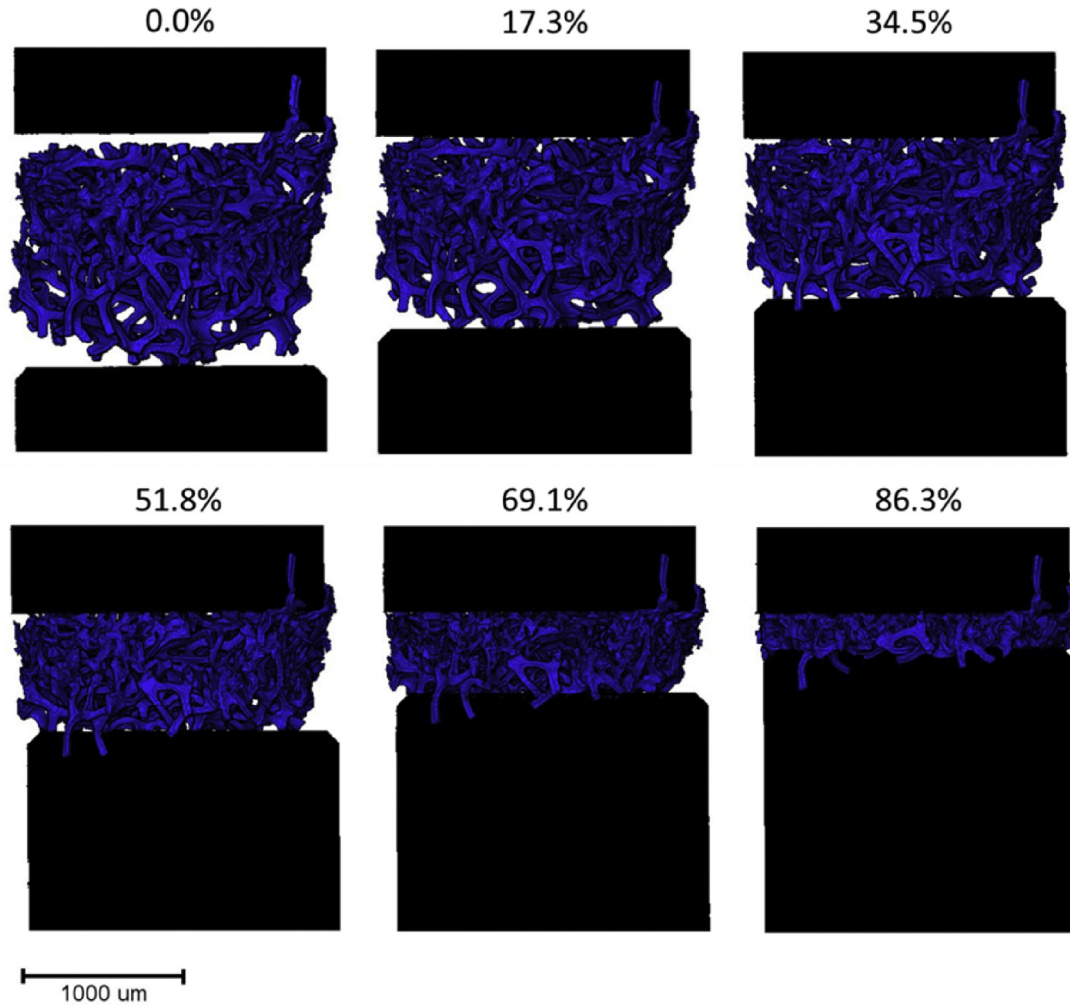

Fig. 4 – Measured foam ICR.

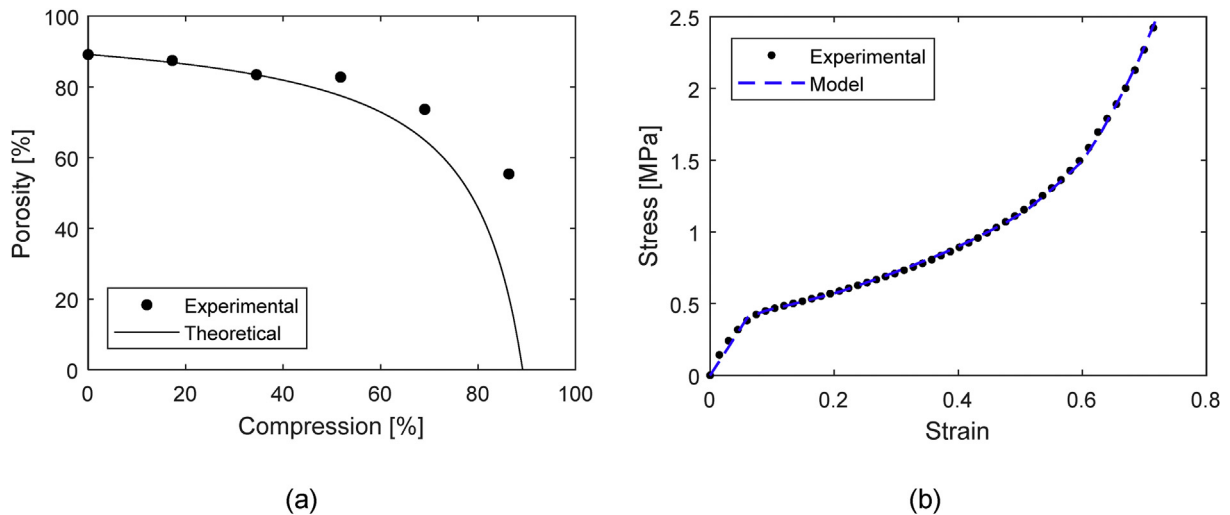Fig. 5 – X-ray CT images of foam under different compression levels.

Fig. 6 – Compression characteristics of metal foam (a) experimental and theoretical porosity at different foam compression, (b) experimental and FEA model stress strain relationship of foam.

scale, the field-of-view was reduced to 523 × 523 × 800 μm in the x, y and z directions, respectively; meaning the full foam flow-field thickness and compressing plates were not captured. Material fraction 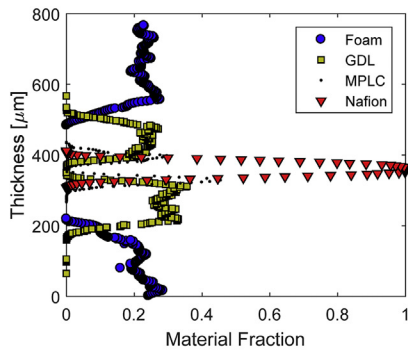analysis for each scan layer in the z-direction is shown in Fig. 7c, d and g for the different compression levels. A material fraction of 1 signifies a solid structure with zero porosity; a value lower than 1 implies either a porous structure or the presence of multiple materials in the same layer.
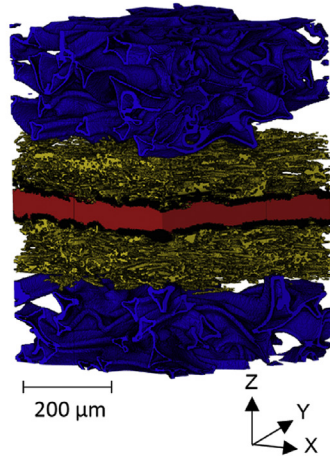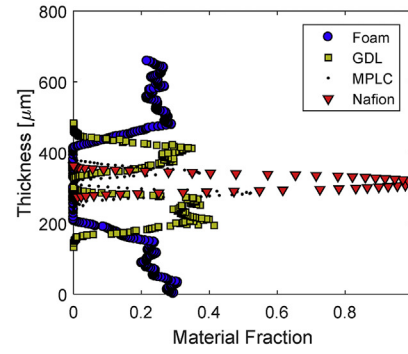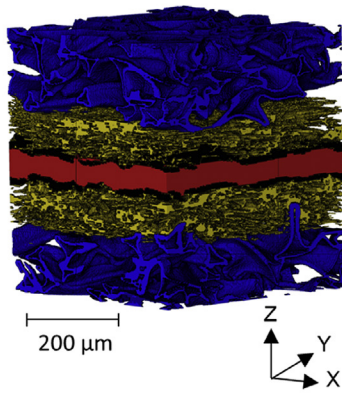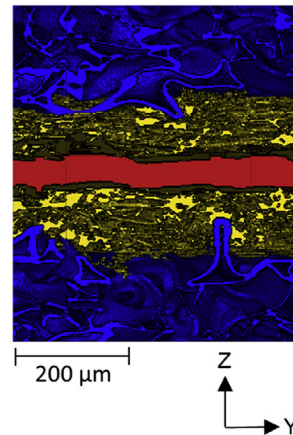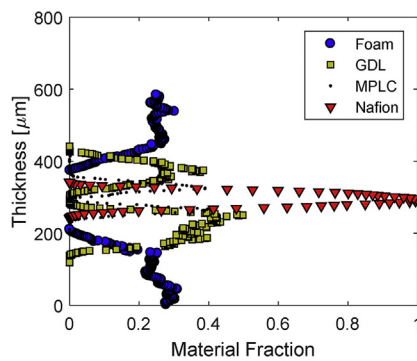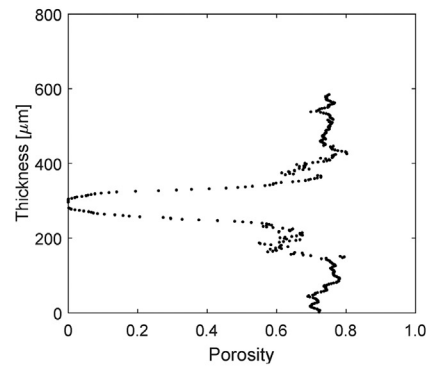
(a)
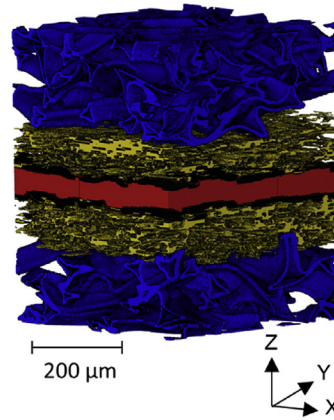
(b)

(c)

(d)

(e)

(f)

(g)

(h)

Table 3 – Component properties at different compression levels, thickness measurements are ±1.7 μm.

Compression	0%	15%	25%
Foam thickness (μm) (in field-of-view)	214.7	207.9	207.9
	281.2	245.3	209.6
GDL thickness (μm)	173.8	148.2	144.9
	155	132.9	124.4
MPLC + Nafion thickness (μm)	143.1	134.6	134.7
Foam to GDL normalised contact area (μm²/μm²)	0.04	0.26	0.41

The high stiffness of the bulk nickel ligament material and large pore size of the foam relative to the GDL lead to intrusion of individual foam ligaments into the GDL under compression. At the maximum 25% compression, foam ligaments are seen to intrude over 50% through the GDL depth (Fig. 7f). Inspection of the material thickness fractions confirms that the foam does not puncture the membrane or catalyst layer. As the ligaments penetrate the GDL, the GDL also fills the open pore volume of the foam, increasing the contact area between the foam and GDL and dispersing the compressive load. This is shown in the increased material fraction overlap. At 25% compression, the normalised interfacial contact area between the foam and GDL was 41%, compared to 4.7% between the foam and stainless-steel compression plate.

The porosity distribution through the thickness of the flow-field and MEA under 25% compression is shown in Fig. 7h. The porosity reduces from 75% in the foam flow-field to 0% at the membrane interface without any step changes in porosity, such as the step between the land and channel flow-field and GDL in a conventional flow-field. The more regular porosity variation of the compressed foam flow-field improves reactant distribution at the catalyst layer compared to the conventional land and channel structure; which are prone to reactant starvation and liquid water accumulation under the land area. Previous studies using metal foam flow-fields have shown improved performance compared to land and channel designs at high current densities where mass transport effects dominate [23].

The thickness of the different components during compression is shown in Table 3, calculated as the thickness containing 98% of the material. The microporous layer/catalyst (MPLC) and Nafion have been considered as a single layer due to material intrusion during hot pressing and the magnitude of MEA undulation compared to the individual layer thickness. Despite the bulk nickel stiffness being significantly greater than the GDL, most of the compression occurs in the foam flow-field and not the MEA. This is caused by lower relative structural stiffness of the open cell foam and pre-compression of the MEA components during hot pressing. The Nafion and MPLC undergo no notable change in thickness under compression, whereas the GDL thickness reduces up to 15% cell compression then only changes by a small amount between 15% and 25% overall compression. To the author's best knowledge, this is the first time a complete MEA, with novel flow field plate, is compressed in-situ.
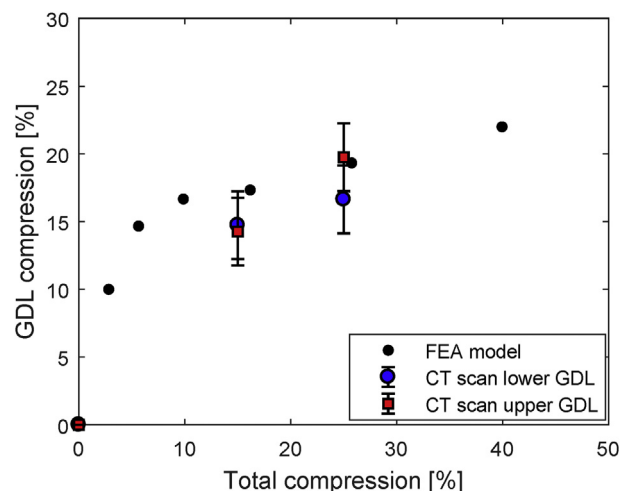
Fig. 8 – Comparison of GDL compression with total compression, experimental and FEA model.

The finite element model, described in Section Finite element model, is used to evaluate the mechanical behaviour of metal foam flow-field fuel cells at the macroscopic cell and stack level. To evaluate the model accuracy, compression of a single MEA and metal foam flow-field were simulated using the same properties and dimensions as the X-ray CT images, without the presence of the MPLC. The GDL compression of both the model and CT scans as a function of total compression is shown in Fig. 8, showing good agreement in both magnitude and gradient. Discrepancies between the model and CT scans are potentially caused by the assumption of a homogenous foam and GDL in the model, ignoring penetration effects, and irreversible compression of the GDL during hot pressing. From the foam compression of Fig. 6b and GDL compression of Fig. 8, it can be concluded that the FEA model provides a suitable representation of macroscopic compressive behaviour in a PEMFC with metal foam flow-fields.

The contact pressure distribution across the interface between the GDL and metal foam flow-field of a 100 cm² active area single fuel cell assembly with sealing gasket is shown in Fig. 9a. The contact pressure distribution for a conventional land and channel flow-field using graphite bipolar plates is shown in Fig. 9b for comparison. In the model, both cells are assembled using an 8-bolt design with endplates of identical geometry and 1.25 kN compressive force per bolt. The metal foam flow-field model exhibits a significant reduction in contact pressure variation across the surface of the MEA compared to the conventional land and channel design. Variation between the maximum and minimum contact pressures was 2.66% for the foam flow-field and 57.41% for the conventional design, excluding the channel areas with no contact. The significant reduction in variation with the foam flow-field is due to plastic deformation of the foam under assembly loads compensating for deflections in the endplates

Fig. 7 – X-ray CT images and analysis of foam flow-field and MEA under compression; (a) 0% compression, (b) 15% compression, (c) 0% compression material fraction, (d) 15% compression material fraction, (e) 25% compression, (f) 25% compression detailed cross section, (g) 25% compression material fraction, (h) 25% compression porosity distribution.

under the clamping force. Under the 12 kN clamping force (1.5 kN per bolt), the maximum and minimum thickness in the foam flow-field were 813.8 μm and 745.8 μm respectively, corresponding to 83.1% and 82.9% porosity.

Whilst plastic deformation during assembly is beneficial for providing even contact pressure distribution, over-torqueing bolts and external impacts can lead to irreversible compression of the foam, reducing porosity and causing irreversible damage to the stack. The effect of increased bolt loads on the stress distribution in the foam and gasket is shown in Fig. 10. The model results demonstrate that once the foam has been compressed to the thickness of the gasket, the load path transitions from the foam to the gasket which has a

higher stiffness. The transition of the load away from the foam reduces the risk of irreversible plastic deformation due to overtightening. This demonstrates how the selection of gasket thickness, stiffness and contact area is essential in controlling flow-field porosity in a metal foam fuel cell.

At operating temperature and humidity, the fuel cell components are subjected to thermal expansion; additionally, the membrane also experiences expansion due to water up-take and a reduction in Young's modulus during operation. Previous studies using a 1D model and conventional flow-fields have demonstrated up to a 15% increase in MEA con-tact pressure during operation [51]. In a fuel cell with metal foam flow-fields, the additional loading during operation
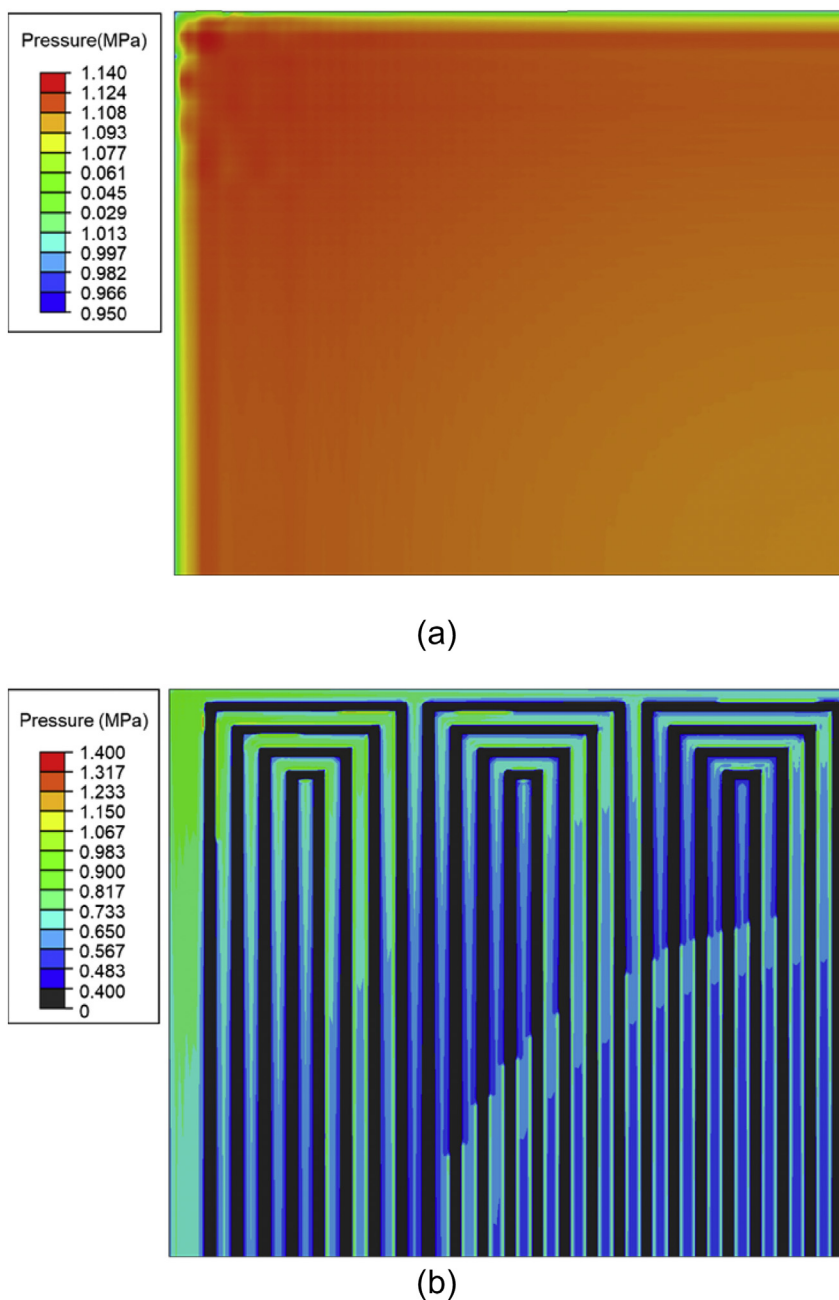

(a)

(b)

Fig. 9 – 1/4 cell (50 × 50 mm) GDL contact pressure distribution in an 8-bolt 100 cm² PEMFC, 1.5 kN per bolt, (a) metal foam flow-field, (b) graphite bipolar plate, (note: different scales).
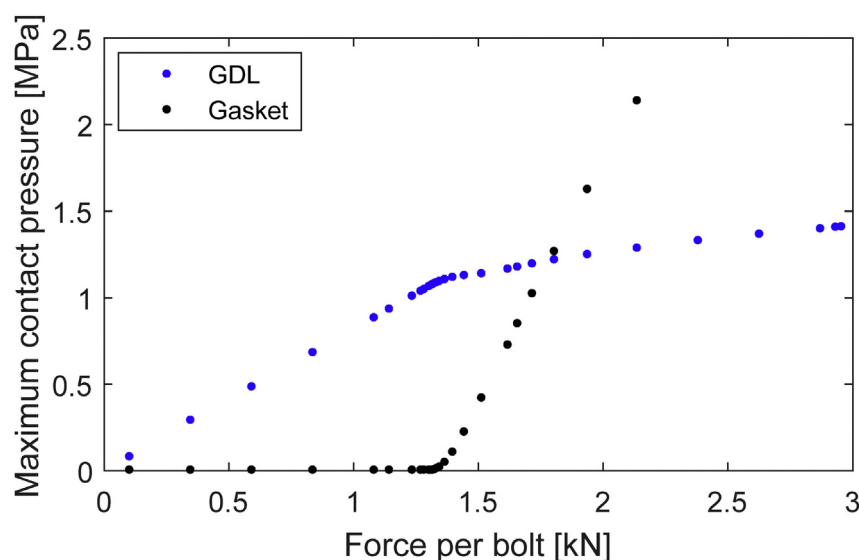
Fig. 10 – **Contact pressure distribution between foam/GDL and BPP/gasket at different compressive loads.**

could lead to further plastic deformation of the foam. Thermal and hydration expansion are represented in the model using the equivalent coefficient of expansion (Eq. (3)) and a look-up table for PEM Young's modulus. When operating conditions of 80 °C at 90% relative humidity are applied to the cell, the maximum GDL contact pressure increased by 2.5% from 1.139 to 1.168 MPa. After returning to 20 °C at 30% relative humidity, the maximum GDL contact pressure reduced to 1.120 MPa, a 29 kPa reduction from the initial assembly condition. Beyond the first operating condition cycle, the foam flow-field exhibits no further plastic deformation, with maximum GDL contact pressure cycling between 1.120 MPa (ambient) and 1.170 MPa (operational). The small amount of hysteresis during the initial cycle is due to the expansion of components plastically deforming the foam. Whilst this is not present in further cycles to the same operating conditions, overheating of the cell may lead to permanent reductions in the compressive force, and hence increase the contact resistance, of the fuel cell.

Simulations on a five-cell fuel cell stack with metal foam flow-fields demonstrate excellent uniformity between cells. Foam-to-GDL contact pressure and foam thickness for each cell are shown in Table 4 for a total clamping load of 12 kN (1.5 kN per bolt). Values for each cell are taken from the GDL and foam furthest away from the stack centre. Due to the symmetry constraint in the xy plane at the centre of the stack, cells 1 and 5 are identical, as are cells 2 and 4. During assembly, the five-cell stack is compressed by a total of 8.5 mm (24%) to enable contact between the BPP and gasket, in a 100-

cell stack this would increase to 170 mm, which would require external compression prior to the clamping method being applied.

Conclusions

The mechanical behaviour of porous metal foam flow-fields has been studied from the micro-scale interaction between foam ligaments and the GDL, to the macro-scale stack level pressure distribution. When the foam flow-fields are compressed in-situ with a membrane electrode assembly, significant penetration of foam ligaments into the carbon paper GDL was seen. This interaction between the foam and GDL results in high normalised contact areas and a continuous porosity distribution profile from the flow-field to the catalyst layer. Increased foam compression lead to improved electrochemical performance caused by a reduction in interfacial contact resistance, although at the expense of mass transport losses. Higher foam compression levels leads to a reduction in cell pitch and hence an increase in volumetric power density.

At the macro cell and stack level, finite element analysis simulations demonstrate that plastic deformation of the foam during compression leads to significantly improved contact pressure distribution across the cell. Thickness control and over-compression protection of the foam flow-field can be avoided through appropriate selection of gasket thickness and stiffness; repeated temperature and humidity cycles are also seen to have a minimal influence on contact pressure.

The findings of this work can be used to optimise porous metal foam flow-fields for improved performance in future PEMFC designs.

Table 4 – Contact pressure and foam thickness of a 5-cell metal foam fuel cell stack.				
Cells		1 and 5	2 and 4	3
Foam to GDL contact	Max	1.109	1.109	1.108
pressure (MPa)	Min	1.087	1.087	1.087
Foam thickness (μm)	Max	811	810.9	810.9
	Min	788.6	788.9	786.5

Appendix

Table 5 – Material properties for the FEA model.

Component	Value
Endplate – Stainless steels	
Width/height	144 mm
Thickness	20 mm
Young's modulus	180 GPa
Poisons ratio	0.3
Thermal expansion	77×10^{-6} K^{-1} [52]
Bipolar plate – Stainless steel (foam cell)	
Width/height	116 mm
Thickness	1 mm
Young's Modulus	180 GPa
Poisson's ratio	0.3
Thermal expansion	77×10^{-6} K^{-1} [52]
Bipolar plate – Graphite (standard flow-field)	
Width/height	106 mm
Thickness	3 mm
Young's modulus	10 GPa
Poisons ratio	0.25
Channel height	1 mm
Channel thickness	1 mm
Number of channels	48
GDL	
Width/height	100 mm
Thickness	200 μm
Young's modulus	Variable [46] (15 MPa@38% strain)
Poisson's ratio	0.25 [48]
Thermal expansion	7.9×10^{-6} K^{-1} [52]
PEM	
Width/height	116 mm
Thickness	50 μm
Young's modulus	Variable [48]
Poisson's ratio	0.4
Thermal expansion	90×10^{-6} K^{-1} [52]
Hydration expansion	0.0115 λ^{-1} [51]
Gasket	
Width/height (outer)	116 mm
Width/height (inner)	100 mm
Thickness	1 mm
Young's modulus	Variable [46] (50 MPa @ 17% strain)
Poisson's ratio	0.3
Thermal expansion	77×10^{-6} K^{-1} [52]
Foam	
Width/height	100 mm
Thickness	1.6 mm
Young's modulus	Variable (this work)
Poisson's ratio	0
Clamp	
Bolt diameter	8 mm
Number of bolts	8
Young's modulus	180 GPa
Poisson's ratio	0.3
Thermal expansion	77×10^{-6} K^{-1} [52]

REFERENCES

[1] Larminie J, Dicks A. Fuel cell systems explained. 2003.

[2] Peng L, Yi P, Lai X. Design and manufacturing of stainless steel bipolar plates for proton exchange membrane fuel cells. Int J Hydrog Energy Dec. 2014;39(36):21127–53.

[3] Ryan O'hayre WGC, Cha Suk-Won. Fuel Cell Fundamentals. 2016.

[4] C. Wang, Q. Zhang, S. Shen, Y. Xiaohui, F. Zhu, and X. Cheng, The respective effect of under-rib convection and pressure drop of flow fields on the performance of PEM fuel cells, Sci Rep 7:43447.

[5] Li X, Sabir I. Review of bipolar plates in PEM fuel cells: flow-field designs. Int J Hydrog Energy 2005;30(4):359–71.

[6] Sasmito AP, Kurnia JC, Mujumdar AS. Numerical evaluation of various gas and coolant channel designs for high performance liquid-cooled proton exchange membrane fuel cell stacks. Energy 2012;44(1):278–91.

[7] Liu H, Li P, Juarez-Robles D, Wang K, Hernandez-Guerrero A. Experimental study and comparison of various designs of gas flow fields to PEM fuel cells and cell stack performance. Front Energy Res 2014;2(January):1–8.

[8] Meyer Q, Ashton S, Jervis R, Finegan DP, Boillat P, Cochet M, Curnick O, Reisch T, Adcock P, Shearing PR, Brett DJL. The hydro-electro-thermal performance of air-cooled, open-cathode polymer electrolyte fuel cells: combined localised current density, temperature and water mapping. Electrochim Acta Oct. 2015;180:307–15.

[9] Meyer Q, Ashton S, Boillat P, Cochet M, Engebretsen E, Finegan DP, Lu X, Bailey JJ, Mansor N, Abdulaziz R, Taiwo OO, Jervis R, Torija S, Benson P, Foster S, Adcock P, Shearing PR, Brett DJL. Effect of gas diffusion layer properties on water distribution across air-cooled, open-cathode polymer electrolyte fuel cells: a combined ex-situ X-ray tomography and in-operando neutron imaging study. Electrochim Acta Sep. 2016;211:478–87.

[10] Mason TJ, Millichamp J, Neville TP, El-kharouf A, Pollet BG, Brett DJL. Effect of clamping pressure on ohmic resistance and compression of gas diffusion layers for polymer electrolyte fuel cells. J Power Sources Dec. 2012;219:52–9.

[11] Kusoglu A, Karlsson AM, Santare MH, Cleghorn S, Johnson WB. Mechanical response of fuel cell membranes subjected to a hygro-thermal cycle. J Power Sources 2006;161(2):987–96.

[12] Yuan W, Tang Y, Yang X, Wan Z. Porous metal materials for polymer electrolyte membrane fuel cells – a review. Appl Energy Jun. 2012;94:309–29.

[13] Trogadas P, Cho JIS, Neville TP, Marquis J, Wu B, Brett DJL, Coppens M-O. A lung-inspired approach to scalable and robust fuel cell design. Energy Environ Sci Jan. 2018;11(1):136–43.

[14] Tan WC, Saw LH, Thiam HS, Xuan J, Cai Z, Yew MC. Overview of porous media/metal foam application in fuel cells and solar power systems. Renew Sustain Energy Rev Nov. 2018;96:181–97.

[15] Lefebvre L-P, Banhart J, Dunand DC. Porous metals and metallic foams: current status and recent developments. Adv Eng Mater Sep. 2008;10(9):775–87.

[16] Mostafid ALI, Medraj M, Lefebvre L. Determination of bulk and entrance contributions to the pressure drop in metallic foams. In: In proceedings of the 5th international conference on porous metals and metallic foams 2007; 2007. 2007-09-05.

[17] Kim GH, Eom KS, Kim MJ, Yoo SJ, Jang JH, Kim HJ, Cho EA. Design of an advanced membrane electrode assembly

employing a double-layered cathode for a PEM fuel cell. ACS Appl Mater Interfaces 2015;7(50):27581–5.

[18] Kim M, Kim C, Sohn Y. Application of metal foam as a flow field for PEM fuel cell stack. Fuel Cells 2018;18(2):123–8.

[19] Murphy OJ, Cisar A, Clarke E. Low-cost light weight high power density PEM fuel cell stack. Electrochim Acta 1998;43(24):3829–40.

[20] Kumar A, Reddy RG. Polymer electrolyte membrane fuel cell with metal foam in the gas flow-field of bipolar/end plates. J New Mater Electrochem Syst 2003;6:231–6.

[21] Kumar A, Reddy RG. Materials and design development for bipolar/end plates in fuel cells,. J Power Sources 2004;129(1):62–7.

[22] Kumar A, Reddy R. Modeling of polymer electrolyte membrane fuel cell with metal foam in the flow-field of the bipolar/end plates. J Power Sources Feb. 2003;114(1):54–62.

[23] Shin DK, Yoo JH, Kang DG, Kim MS. Effect of cell size in metal foam inserted to the air channel of polymer electrolyte membrane fuel cell for high performance. Renew Energy 2017;115:663–75.

[24] Huo S, Cooper NJ, Smith TL, Park JW, Jiao K. Experimental investigation on PEM fuel cell cold start behavior containing porous metal foam as cathode flow distributor. Appl Energy Oct. 2017;203:101–14.

[25] Tabe Y, Nasu T, Morioka S, Chikahisa T. Performance characteristics and internal phenomena of polymer electrolyte membrane fuel cell with porous flow field. J Power Sources 2013;238:21–8.

[26] Jo A, Ahn S, Oh K, Kim W, Ju H. Effects of metal foam properties on flow and water distribution in polymer electrolyte fuel cells (PEFCs). Int J Hydrog Energy 2018;43:14034–46.

[27] Tsai B-T, Tseng C-J, Liu Z-S, Wang C-H, Lee C-I, Yang C-C, Lo S-K. Effects of flow field design on the performance of a PEM fuel cell with metal foam as the flow distributor. Int J Hydrog Energy 2012;37(17):13060–6.

[28] Fly A, Butcher D, Meyer Q, Whiteley M, Spencer A, Kim C, Shearing PR, Brett DJL, Chen R. Characterisation of the diffusion properties of metal foam hybrid flow- fields for fuel cells using optical flow visualisation and X-ray computed tomography. J Power Sources 2018;395(January):171–8.

[29] Jo A, Ju H. Numerical study on applicability of metal foam as flow distributor in polymer electrolyte fuel cells (PEFCs). Int J Hydrog Energy Jul. 2018;43(30):14012–26.

[30] Lee Y-H, Li S-M, Tseng C-J, Su C-Y, Lin S-C, Jhuang J-W. Graphene as corrosion protection for metal foam flow distributor in proton exchange membrane fuel cells. Int J Hydrog Energy Apr. 2017;42(34):22201–7.

[31] Sim Y, Kwak J, Kim S-Y, Jo Y, Kim S, Kim SY, Kim JH, Lee C-S, Jo JH, Kwon S-Y. "Formation of 3D graphene–Ni foam heterostructures with enhanced performance and durability for bipolar plates in a polymer electrolyte membrane fuel cell. J Mater Chem A Jan. 2018;6(4):1504–12.

[32] Rama P, Liu Y, Chen R, Ostadi H, Jiang K, Gao Y, Zhang X, Fisher R, Jeschke M. Simulation of liquid water breakthrough in a nanotomography reconstruction of a carbon paper gas-diffusion layer. Am Inst Chem Eng J 2012;58(2):646–55.

[33] Gao Y, Zhang X, Rama P, Chen R, Ostadi H, Jiang K. "Lattice Boltzmann simulation of water and gas flow in porous gas diffusion layers in fuel cells reconstructed from micro-tomography. Comput Math Appl 2013;65(6):891–900.

[34] Rama P, Liu Y, Chen R, Ostadi H, Jiang K, Gao Y, Zhang X, Brivio D, Grassini P. A numerical study of structural change and anisotropic permeability in compressed carbon cloth polymer electrolyte fuel cell gas diffusion layers. Fuel Cells 2011;11(2):274–85.

[35] Jinuntuya F, Whiteley M, Chen R, Fly A. The effects of gas diffusion layers structure on water transportation using X-

[36] Hack J, Heenan TMM, Iacoviello F, Mansor N, Meyer Q, Shearing P, Brandon N, Brett DJL. A structure and durability comparison of membrane electrode assembly fabrication methods: self-assembled versus hot-pressed. J Electrochem Soc 2018;165(6):F3045–52.

[37] James JP, Choi HW, Pharoah JG. X-ray computed tomography reconstruction and analysis of polymer electrolyte membrane fuel cell porous transport layers. Int J Hydrog Energy 2012;37(23):18216–30.

[38] Zenyuk IV, Parkinson DY, Connolly LG, Weber AZ. Gas-diffusion-layer structural properties under compression via X-ray tomography. J Power Sources 2016;328:364–76.

[39] Kotaka T, Tabuchi Y, Mukherjee PP. Microstructural analysis of mass transport phenomena in gas diffusion media for high current density operation in PEM fuel cells. J Power Sources 2015;280:231–9.

[40] Holzer L, Pecho O, Schumacher J, Marmet P, Stenzel O, Büchi FN, Lamibrac A, Münch B. Microstructure-property relationships in a gas diffusion layer (GDL) for Polymer Electrolyte Fuel Cells, Part I: effect of compression and anisotropy of dry GDL. Electrochim Acta 2017;227:419–34.

[41] Fazeli M, Hinebaugh J, Fishman Z, Tötzke C, Lehnert W, Manke I, Bazylak A. Pore network modeling to explore the effects of compression on multiphase transport in polymer electrolyte membrane fuel cell gas diffusion layers. J Power Sources 2016;335:162–71.

[42] Tötzke C, Gaiselmann G, Osenberg M, Bohner J, Arlt T, Markötter H, Hilger A, Wieder F, Kupsch A, Müller BR, Hentschel MP, Banhart J, Schmidt V, Lehnert W, Manke I. Three-dimensional study of compressed gas diffusion layers using synchrotron X-ray imaging. J Power Sources 2014;253:123–31.

[43] Meyer Q, Mansor N, Iacoviello F, Cullen PL, Jervis R, Finegan D, Tan C, Bailey J, Shearing PR, Brett DJL. Investigation of hot pressed polymer electrolyte fuel cell assemblies via X-ray computed tomography. Electrochim Acta 2017;242:125–36.

[44] ASTM. Standard test method for flatwise compressive properties of sandwich cores 1, i. "; 2011. p. 1–8.

[45] El-Kharouf A, Mason TJ, Brett DJL, Pollet BG. Ex-situ characterisation of gas diffusion layers for proton exchange membrane fuel cells. J Power Sources 2012;218:393–404.

[46] Ismail MS, Hassanpour A, Ingham DB, Ma L, Pourkashanian M. On the compressibility of gas diffusion layers in proton exchange membrane fuel cells. Fuel Cells Jun. 2012;12(3):391–7.

[47] Tang Y, Karlsson AM, Santare MH, Gilbert M, Cleghorn S, Johnson WB. An experimental investigation of humidity and temperature effects on the mechanical properties of perfluorosulfonic acid membrane. Mater Sci Eng, A Jun. 2006;425(1–2):297–304.

[48] Zhou Y, Lin G, Shih AJ, Hu SJ. Assembly pressure and membrane swelling in PEM fuel cells. J Power Sources Jul. 2009;192(2):544–51.

[49] Ashby MF, Evans A, Fleck NA, Gibson LJ, Hutchinson JW, Wadley HNG. Metal Foams: a design guide. Butterworth-Heinemann; 2000.

[50] Millichamp J, Mason TJ, Neville TP, Rajalakshmi N, Jervis R, Shearing PR, Brett DJL. Mechanisms and effects of mechanical compression and dimensional change in polymer electrolyte fuel cells – a review. J Power Sources Jun. 2015;284:305–20.

[51] Fly A, Chen R, Wang X. Equivalent stiffness model of a proton exchange membrane fuel cell stack including hygrothermal effects and dimensional tolerances. J Electrochem Energy Convers Storage 2018;15(3):031002.

[52] Lin P, Zhou P, Wu CW. A high efficient assembly technique for large proton exchange membrane fuel cell stacks: Part II. Applications. J Power Sources Mar. 2010;195(5):1383–92.